ELSEVIER

Journal of Fluids and Structures 20 (2005) 927–948

JOURNAL OF FLUIDS AND STRUCTURES

www.elsevier.com/locate/jfs

Linear and nonlinear analyses of sheet flutter induced by leakage flow

X. Wu, S. Kaneko*

Department of Mechanical Engineering, University of Tokyo, 7-3-1, Hongo, Bunkyo-ku, Tokyo, 113-8656, Japan

Received 29 September 2004; accepted 7 May 2005

Abstract

This paper deals with both linear and nonlinear analyses of sheet flutter in a narrow passage caused by fluid–structure interaction. The sheet is considered as a combination of massless beam elements, springs and discrete mass particles, in which the mass of each particle and spring coefficients are calculated based on the beam model. In the linear analysis, equations of motion of the system are obtained by formulating fluid dynamic forces and moments acting on each sheet element, yielding an eigenvalue problem. To show the validity of the proposed method, calculated results were compared with previously reported experimental ones. In the nonlinear analysis, nonlinear fluid dynamic forces are introduced to simulate the behavior of the sheet, showing the appearance of limit-cycle vibration in high flow speed.

Keywords: Flow induced vibration; Flutter; Stability; Leakage flow; Eigenvalue analysis; Nonlinear analysis; Discretized beam model

1. Introduction

It is known that flutter or divergence of a travelling sheet may occur during its manufacturing process under the influence of leakage flow between the travelling sheet and a guide. In order to avoid quality defects like wrinkles due to such unsteady phenomena happening on the sheet, it is important to evaluate the fluid dynamic force and moment acting on the sheet for predicting sheet behavior. As a practical problem, steel strip flutter can occur during manufacturing when producers want to improve the production efficiency by increasing the speed of the traveling steel strips. To study the instability of travelling sheets, Yamaguchi et al. (1999a,b) performed a theoretical stability analysis of a thin sheet subjected to high speed flow by computing the fluid dynamic force corresponding to small perturbed sheet motion based on the vibrating wing theory, and carried out wind tunnel experiments to obtain the critical flow speed, flutter mode and flutter frequency. In later research by Yamaguchi et al. (2003), the theoretical flutter limit mainly influenced by the ratio of tension to bending stiffness was discussed, and the experimental flutter limit obtained in the wind tunnel was found on the average to agree with the theoretical one for the tested range. Nakashima et al. (1999) developed a 2-D sheet model in 3-D flow for simulation of sheet flutter, where it was reported that the critical flow speed is approximately proportional to the oncoming flow speed. Chang and Moretti (2000) studied the flutter phenomenon using a simplified pattern of sheet motion and successfully computed both the critical flow speed and flutter frequency, showing agreement with experimental results only in a qualitative sense. Furthermore, Watanabe

*Corresponding author.
E-mail address: kaneko@mech.t.u-tokyo.ac.jp (S. Kaneko).

0889-9746/$ - see front matter © 2005 Elsevier Ltd. All rights reserved.
doi:10.1016/j.jfluidstructs.2005.05.008

Nomenclature

b	width of sheet and passage
c_i	damping coefficient of damper connecting element i and element $i+1$
C_Q	integration constant, function of time t
f_{zi}	nondimensional fluid force acting on discrete ith mass particle
E	Young's modulus for sheet
F_i	fluid force acting on discrete ith mass particle
h, $\bar{h}$	height of leakage passage, average height of leakage passage, respectively
h_c	displacement from element center c to lower wall
Δh	translational vibration amplitude
I	moment of inertia of sheet, $I = bt_s^3/12$
k_i	stiffness of rotational spring connecting element i and element $i+1$
l	length of one element of sheet or leakage flow length
L	length of sheet
m_i	mass of element i of sheet
n	number of elements
P, $\bar{P}$	pressure, steady pressure, respectively
ΔP, p	fluctuating pressure, nondimensional fluctuating pressure, respectively
Q, $\bar{Q}$	flow rate, steady flow rate, respectively, $\bar{Q} = b\bar{h}V_{\text{air}}$
ΔQ, q	fluctuating flow rate, nondimensional fluctuating flow rate, respectively
t	time
t_s	thickness of sheet
V_{air}	average leakage flow velocity
V_{crit}	critical flow velocity
V^*_{crit}	nondimensional critical flow velocity
X, x	nondimensional displacement in x direction, displacement in x direction, respectively, $X = x/l$
z	displacement in z direction
η	nondimensional amplitude of translational vibration, $\eta = \Delta h/\bar{h}$
Θ	nondimensional amplitude of rotational vibration, $\Theta = l\Delta\theta_0 h/\bar{h}$
$\Delta\theta_0$	rotational vibration amplitude
λ	friction coefficient of wall
μ	viscosity of fluid
μ_m	mass ratio, $\mu_m = \rho_m/(\rho bL)$
v	kinematic viscosity of fluid
ξ_{in}, ξ_{ex}	pressure loss coefficient at the inlet and outlet of passage, respectively
ρ	density of fluid
ρ_m	mass per unit length of sheet
ϕ_i	rotational angle of ith sheet element measured from x-axis
Ω, ω	angular frequency, nondimensional angular frequency, respectively

et al. (2002a,b) developed a Navier-Stokes simulation and a potential flow analysis for investigation of paper flutter, and also performed experiments. By comparison among results obtained from two different methods and experiments, the potential flow analysis, which needs less time and computation resources, proves effective and adaptable for a parametric study.

The investigations mentioned above are all concerned with sheet flutter in unconfined space. In reality, the behavior of travelling sheet is influenced by adjoining boundaries, such as guides or covers of the machine. Therefore, studies on the sheet subjected to a narrow leakage flow are required.

Concerning unsteady vibrations of a continuum subjected to a leakage flow, Nagakura and Kaneko (1992) analyzed the unstable behavior of a cantilever beam by employing the modal analysis method, and they compared the results obtained with experimental results. The objective is limited to an elastic beam that has high stiffness compared with the influence of the fluid dynamic force acting on the beam. As an extension of the study mentioned above, Kaneko et al. (2000) investigated sheet flutter under the effect of tension acting on the fixed ends of the sheet. Utilizing a beam model and employing a finite element method, a stability analysis was carried out and its appropriateness was confirmed by comparing with experimental data. It was concluded that a reliable result was obtained in the case where the shape function of the beam element is described by analytical functions. However, we find it difficult to apply the above methods to some complex conditions such as the cases that need consideration of shearing forces acting on the surface of the sheet or frictional forces acting at the supports. Therefore, we need to develop a more general method of analysis to deal with these kinds of complex conditions.

Moreover, up to now all the studies about sheet flutter focus on the very small amplitude vibration of the sheet without consideration of nonlinear fluid- dynamic behavior in the range of super-critical flow velocities. In contrast, as an instance of nonlinear analysis of fluid–structure coupled problems originating from flow in a narrow passage, Antunes (2002) applied Reynolds' equations to a rotor-dynamics problem in which the rotor is supported by the leakage flow sandwiched in-between the rotor and the bearing. With linearized fluid–structure coupled equations of

motion, the influences of parameters on rotor stability were investigated. Furthermore, by way of calculating the time-history behavior of the system while taking account of nonlinear effect of the fluid force in the case of large-amplitude vibration of the rotor, the necessity of nonlinear analysis was discussed. In addition, Yadykin et al. (2001) applied Galerkin's method for modelling a fluid–strip system, and studied the linear/nonlinear behavior of the strip with varying flow velocity.

In this paper, as an expansion of the spring–mass model for the sheet proposed by Yoshida (1997), a new method for analyzing fluid–structure coupled systems that may be applied in more complicated cases is proposed. Concretely, the sheet subjected to a leakage flow on both sides is regarded as a combination of massless beam elements, springs and discrete mass particles. Coupling with the fluid dynamic forces and moments acting on each sheet element, the equation of motion taking account of the effect of fluid dynamic force and moment is linearized, which results in an eigenvalue analysis. Furthermore, for predicting the unstable nonlinear behavior of the sheet beyond the critical flow speed, a nonlinear analysis of the fluid force is performed.

2. Formulation of the structural equation of motion

The objective for the analysis is shown in Fig. 1. A sheet with the upstream end fixed and the other end free is subjected to a leakage flow on both surfaces. The oncoming air-flow from the inlet of the passage flows into the leakage passage in the x direction with speed V_{air}. As shown in Fig. 2, the sheet is regarded as a discrete beam model consisting of n mass particles, dampers and rotational springs, where l_i and ϕi, denote, respectively, the length of a sheet element and rotational angle measured relative to the x-axis, and we chose $l_1 = l_2 = \cdots = l_n = l$ (constant).

From Fig. 3 we can formulate the mass m_i of the ith particle and stiffness k_i of the spring that connects two adjoining sheet elements, based on the deformation of the tiny cantilever elements. When the moment M is acting on both sides of

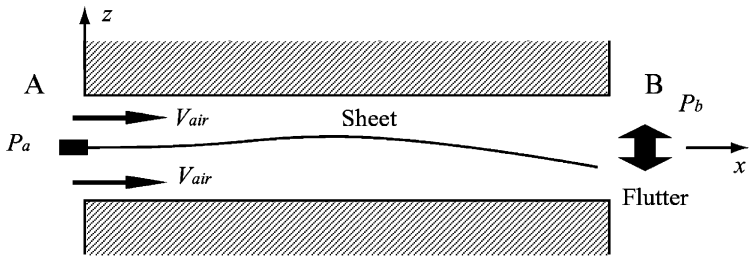

Fig. 1. System under consideration.

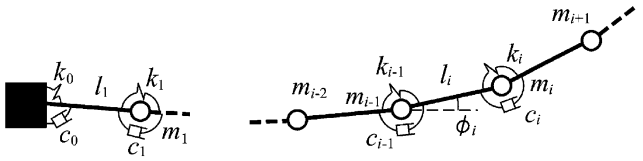

Fig. 2. Modelling of the sheet.

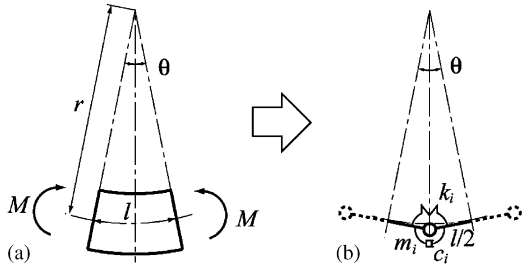

Fig. 3. Modelling of single beam element.

a small element of length l as shown in Fig. 3(a), the radius of curvature of the beam r may be determined by the following equation:

$$\frac{1}{r} = \frac{M}{EI}. \tag{1}$$

Substituting $r = l/\theta$ into Eq. (1) results in

$$\frac{M}{\theta} = \frac{EI}{l}. \tag{2}$$

On the other hand, because the stiffness of the spring illustrated in Fig. 3(b) is defined as $k_i = M/\theta$, we substitute it into Eq. (2) to formulate an equation for the stiffness k_i:

$$k_i = EI/l. \tag{3}$$

Additionally, as shown in Fig. 3, the discrete mass m_i equal to the mass of the beam element is defined as

$$m_i = \rho_m l, \tag{4}$$

where ρ_m denotes mass per length of the beam.

It is assumed that the damping moment acting on the ith sheet is proportional to the difference of angular velocities of two adjoining elements:

$$M_{ci} = -c_i(\dot{\phi}_{i+1} - \dot{\phi}_i). \tag{5}$$

Furthermore, the position of the ith particle (x_i , z_i) may be given from the geometric relationship

$$x_i = \sum_{j=1}^{i} l \cos \phi_j,\ z_i = \sum_{j=1}^{i} l \sin \phi_j.$$

Then, the Lagrangian and Lagrange's equation for the beam become

$$L = \sum_{i=1}^{n} \frac{m_i}{2}(\dot{x}_i^2 + \dot{z}_i^2) - \sum_{i=0}^{n-1} \frac{k_i}{2}(\phi_{i+1} - \phi_i)^2 \tag{6}$$

$$\frac{\mathrm{d}}{\mathrm{d}t}\left(\frac{\partial L}{\partial \dot{\phi}_i}\right) - \frac{\partial L}{\partial \phi_i} + \frac{\partial R}{\partial \dot{\phi}_i} = 0 \quad (i = 1, 2, \ldots, n), \tag{7}$$

where R is Rayleigh's dissipation function associated with dissipation:

$$R = \sum_{i=1}^{n} \frac{1}{2} c_i(\dot{\phi}_{i+1} - \dot{\phi}_i)^2. \tag{8}$$

Substituting Eqs. (6)–(8) into Lagrange's equation and linearizing, the following equation of motion is obtained:

$$[J_M]\{\ddot{\boldsymbol{\phi}}\} + [C_M]\{\dot{\boldsymbol{\phi}}\} + [K_M]\{\boldsymbol{\phi}\} = \{\mathbf{Q_z}\} + \{\mathbf{Q_r}\}, \tag{9}$$

where $[J_M]$denotes an $n \times n$ symmetric matrix, $[C_M]$ and $[K_M]$are $n \times n$ tridiagonal symmetric matrices,and $\{\mathbf{Q_z}\}$ and $\{\mathbf{Q_r}\}$ are generalized force vectors contributed by fluid pressure and friction acting on the sheet, respectively. Besides, the elements of vectors and matrices in Eq. (7) are defined by

$$\{\ddot{\boldsymbol{\phi}}\} = \{\ddot{\phi}_1 \quad \ddot{\phi}_2 \quad \cdots \quad \ddot{\phi}_n\}^{\mathrm{T}},\ \{\dot{\boldsymbol{\phi}}\} = \{\dot{\phi}_1 \quad \dot{\phi}_2 \quad \cdots \quad \dot{\phi}_n\}^{\mathrm{T}},\ \{\boldsymbol{\phi}\} = \{\phi_1 \quad \phi_2 \quad \cdots \quad \phi_n\}^{\mathrm{T}}$$

$$\{\mathbf{Q_z}\} = \{Q_{z1} \quad Q_{z2} \quad \cdots \quad Q_{zn}\}^{\mathrm{T}},\ \{\mathbf{Q_r}\} = \{Q_{r1}, Q_{r2}, \cdots Q_{rn}\}^{\mathrm{T}}$$

3. Linear analysis

3.1. Basic equation of leakage flow

The flow in a narrow passage of length l and height h shown in Fig. 4 is discussed here. The flow is assumed to be 2-D, incompressible and viscous. Under this simplification, using the continuity and Navier–Stokes equations for the flow, we can derive another type of formulation for the continuity and momentum equation of leakage flow described by the

volumetric flow rate Q and the height h shown as Eqs. (10) and (11):

$$\frac{\partial Q}{\partial x}+\frac{\partial h}{\partial t}=0, \tag{10}$$

$$\frac{\partial Q}{\partial t}+\frac{\partial}{\partial x}\left(\frac{Q^2}{h}\right)=-\frac{h}{\rho}\frac{\partial P}{\partial x}-\frac{\lambda}{4}\frac{Q^2}{h^2}, \tag{11}$$

where λ is a friction coefficient of wall and may be expressed as a function of Reynolds number as $\lambda=48/\mathrm{Re}$, $\mathrm{Re}=|Q|/v$ in the case of laminar flow, and $\lambda=0.28/\mathrm{Re}^{1/4}$ in the case of turbulent flow. The derivation of these equations is given in the paper by Inada and Hayama (1987); see also Paidoussis (2003).

In addition to the equations governing the fluid flow, the boundary conditions at the inlet and outlet of the flow passage are given by

$$P(-l/2)=P_{in}-\xi_{in}\frac{\rho}{2}\frac{Q^2(-l/2)}{h^2(-l/2)}, \tag{12}$$

$$P(l/2)=P_{ex}+\xi_{ex}\frac{\rho}{2}\frac{Q^2(l/2)}{h^2(l/2)}, \tag{13}$$

where ξ_{in} and ξ_{ex} are pressure loss coefficients at the inlet and outlet of passage, respectively, values for which are dependent on the shape of the inlet and outlet. In this paper, we assume that both the inlet and outlet have a smooth shape, leading to $\xi_{in}=1$ (dynamic pressure loss is included) and $\xi_{ex}=0$.

3.2. Steady pressure and flow rate

In Fig. 4, when both the upper and lower walls are fixed, i.e. the height of leakage passage is kept constant, $Q=\bar{Q}=$const. may be derived from Eq. (10). Substituting $Q=\bar{Q}$ into Eq. (11) and applying the boundary conditions

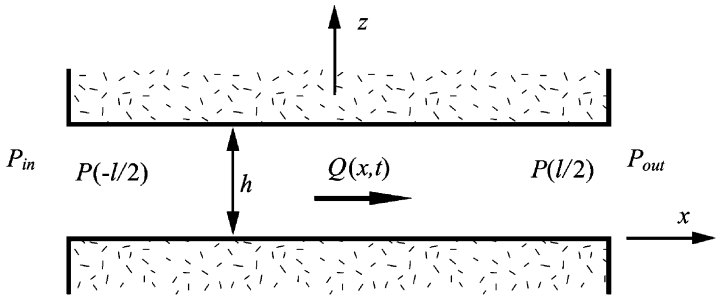

Fig. 4. Leakage flow.

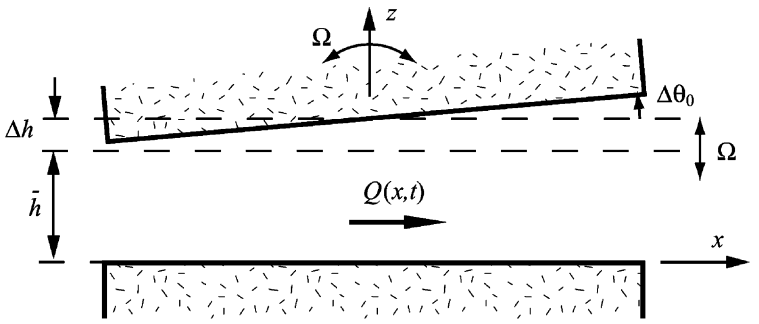

Fig. 5. Geometry of leakage flow with a vibrating side wall.

of Eqs. (12) and (13), the steady pressure $\bar{P}(x)$ and flow rate $\bar{Q}$ may be expressed as a function of the pressure difference between inlet and outlet of passage ($P_{in} - P_{ex}$).

3.3. Unsteady pressure and flow rate

In this paper, it is assumed that the motion of a discrete beam element consists of translational and rotational motion as shown in Fig. 5, i.e. the upper wall translationally vibrates around the equilibrium height $\bar{h}$ with angular frequency Ω and amplitude Δh, and it simultaneously vibrates rotationally around the central point c of the upper wall with the same angular frequency Ω and amplitude $\Delta\theta_0$.

Assuming that the height h, pressure P and flow rate Q change with angular frequency Ω, then, h, P and Q can be described as

$$h(x,t) = \bar{h} + (\Delta h + x\Delta\theta_0)\mathrm{e}^{\mathrm{i}\Omega t}, \quad P(x,t) = \bar{P}(x) + \Delta P(x)\mathrm{e}^{\mathrm{i}\Omega t}, \quad Q(x,t) = \bar{Q} + \Delta Q(x)\mathrm{e}^{\mathrm{i}\Omega t}. \tag{14-16}$$

After substituting Eqs. (14) and (16) into Eq. (10) and then integrating with respect to x, the amplitude of the fluctuating flow rate $\Delta Q(x)$ may be expressed in nondimensional form as

$$q(X) = -\mathrm{i}\omega\left(\eta X + \frac{1}{2}\Theta X^2 + \frac{\eta}{2} - \frac{\Theta}{8}\right) + q\left(-\frac{1}{2}\right), \tag{17}$$

where the nondimensional variables in Eq. (17) are defined as

$$X = x/l, \quad q = \Delta Q/\bar{Q}, \quad \eta = \frac{\Delta h}{\bar{h}}, \quad \Theta = \frac{l}{\bar{h}}\Delta\theta_0, \quad \omega = \frac{l\bar{h}}{\bar{Q}}\Omega,$$

and $q(-1/2)$ is the normalized fluctuating flow rate at inlet, and it is determined by Eq. (21).

Introducing the nondimensional variables defined above into the boundary conditions, Eqs. (12) and (13), the corresponding boundary conditions for the unsteady component of pressure can be expressed by the following equations:

$$p\left(-\frac{1}{2}\right) = -\xi_{\mathrm{in}}\left[2q\left(-\frac{1}{2}\right) - 2\eta + \Theta\right], \tag{18}$$

$$p\left(\frac{1}{2}\right) = \xi_{\mathrm{ex}}\left[2q\left(\frac{1}{2}\right) - 2\eta - \Theta\right], \tag{19}$$

where p is normalized fluctuating pressure defined as $p = \Delta P(x)/(\rho\bar{Q}^2/2\bar{h}^2)$. Substituting Eqs. (14)–(17) into Eq. (11) and integrating with respect to x, the unsteady pressure distribution along the sheet element in nondimensional form can be obtained as

$$\begin{aligned} p(X) = {} & \left[\left(\frac{X^3}{3} - \frac{X}{4} - \frac{1}{12}\right)(\mathrm{i}\omega)^2 + \left\{\frac{l\lambda}{\bar{h}}\left(\frac{X^3}{6} - \frac{X}{8} - \frac{1}{24}\right) + 2X^2 - \frac{1}{2}\right\}(\mathrm{i}\omega) + \left(\frac{3l\lambda}{4\bar{h}}X^2 + 2X - \frac{3\lambda l}{16\bar{h}} + 1 - \xi_{in}\right)\right]\Theta \\ & + \left[\left(X^2 + X + \frac{1}{4}\right)(\mathrm{i}\omega)^2 + \left\{\frac{l\lambda}{2\bar{h}}\left(X^2 + X + \frac{1}{4}\right) + 2 + 4X\right\}(\mathrm{i}\omega) + \left(\frac{3\lambda l}{2\bar{h}}X + \frac{3\lambda l}{4\bar{h}} + 2\xi_{in}\right)\right]\eta \\ & - \left[(2X+1)(\mathrm{i}\omega) + \left(2X + \frac{\lambda l}{2\bar{h}} + 2\xi_{in}\right)\right]q\left(-\frac{1}{2}\right) + C, \end{aligned} \tag{20}$$

where C denotes an integration constant, which is determined by the boundary conditions, as will be seen in what follows.

Coupling Eqs. (18)–(20), $q(-1/2)$ and C may be obtained:

$$\begin{aligned} q\left(-\frac{1}{2}\right) = {} & \frac{1}{2\mathrm{i}\omega + l\lambda/\bar{h} + 2\xi_{in} + 2\xi_{ex}}\left\{\left[4 + 2\xi_{ex} + \frac{1}{2}\left(2\mathrm{i}\omega + \frac{l\lambda}{\bar{h}}\right)\right]\mathrm{i}\omega\eta \right. \\ & \left. - \frac{1}{12}\left(2\mathrm{i}\omega + \frac{l\lambda}{\bar{h}}\right)\mathrm{i}\omega\Theta + (2 - \xi_{in} + \xi_{ex})\Theta + \left(2\xi_{in} + 2\xi_{ex} + \frac{3l\lambda}{2\bar{h}}\right)\eta\right\}, \end{aligned} \tag{21}$$

$$\begin{aligned} C = {} & \left[2 + \frac{1}{4}\left(\mathrm{i}\omega + \frac{\lambda l}{2\bar{h}}\right)\right]\mathrm{i}\omega\eta - \left[\frac{1}{2} + \frac{1}{12}\left(\mathrm{i}\omega + \frac{\lambda l}{2\bar{h}}\right)\right]\mathrm{i}\omega\Theta - \left(\mathrm{i}\omega + \frac{\lambda l}{2\bar{h}} + 2\xi_{in}\right)q\left(-\frac{1}{2}\right) \\ & - \left(\frac{3\lambda l}{16\bar{h}} - 1 + \xi_{in}\right)\Theta + \left(\frac{3\lambda l}{4\bar{h}} + 2\xi_{in}\right)\eta. \end{aligned} \tag{22}$$

As one can easily find from Eq. (20), it is obvious that the unsteady pressure $p(X)$ can be expressed as a function of the rotational vibration amplitude Θ, translational vibration amplitude η, fluctuating flow rate $q(-1/2)$ at the inlet of the sheet element and the integration constant C.

3.4. Fluid force acting on a discrete sheet element

Now, based on the unsteady pressure distribution derived above, we can calculate the fluid force acting on a discrete sheet element subjected to leakage flow. As shown in Fig. 6, when a sheet element vibrates at angular frequency Ω in the translational direction with amplitude Δh_i and in the rotational direction with amplitude $\Delta\theta_0$ simultaneously, the pressure in the lower passage can be calculated by following the procedure discussed above. Due to symmetry of the system, the pressure in the upper passage has the same fluctuating amplitude but the opposite phase as that in the lower passage. Thus, the sum of nondimensional fluctuating pressure acting on the sheet element becomes twice as much as the fluctuating pressure obtained by Eq. (20).

In what follows we discuss the formulation of the fluid force from the pressure. As shown in Fig. 7, summation of the normalized pressure acting on the ith element $p_i(X)$ produces normalized forces f_{i+} and f_{i-} acting on both ends of the element, which may be formulated by considering the balance of moments acting on the element as

$$f_{i+} = 2\int_{-1/2}^{1/2} p_i(X)\left(\frac{1}{2}+X\right)\mathrm{d}X \quad \text{and} \quad f_{i-} = 2\int_{-1/2}^{1/2} p_i(X)\left(\frac{1}{2}-X\right)\mathrm{d}X. \tag{23,24}$$

Thus, the force acting on the ith mass particle f_{zi} is a superposition of the force f_{i+} produced by the pressure acting on the ith element and the force $f_{(i+1)-}$ produced by the pressure acting on the $(i+1)$th element. Formulating the forces acting on all mass particles yields

$$\{\mathbf{f_z}\} = 2\left\{\int_{-1/2}^{1/2}\{\mathbf{p}(X)\}\left(\frac{1}{2}+X\right)\mathrm{d}X + [L_1]\int_{-1/2}^{1/2}\{\mathbf{p}(X)\}\left(\frac{1}{2}-X\right)\mathrm{d}X\right\}, \tag{25}$$

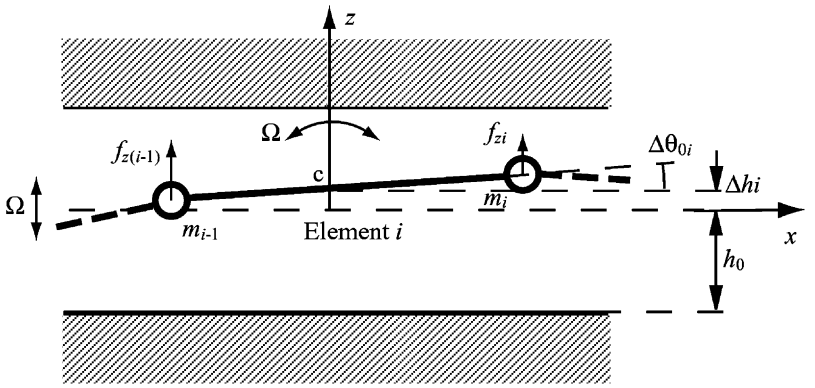

Fig. 6. Motion of an element in linear analysis.

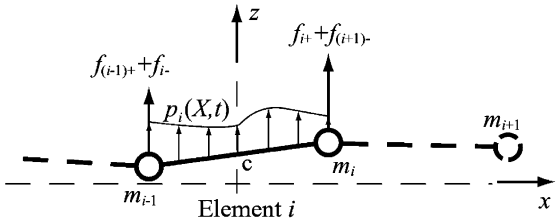

Fig. 7. Fluid forces acting on each particle.

where

$$\{\mathbf{f_z}\} = \begin{Bmatrix} f_{z1} & f_{z2} & \cdots & f_{zn} \end{Bmatrix}^{\mathrm{T}}, \quad \{\mathbf{p}(X)\} = \begin{Bmatrix} p_1(X) & p_2(X) & \cdots & p_n(X) \end{Bmatrix}^{\mathrm{T}},$$

and $[L_1]$ is $n \times n$ matrix (refer to Appendix A).

Substituting Eq. (20) into Eq. (25) leads to the following equation of $\{\mathbf{f_z}\}$:

$$\{\mathbf{f_z}\} = \left(\begin{bmatrix} J_{f11} & J_{f12} & 0 & 0 \end{bmatrix} (\mathrm{i}\omega)^2 + \begin{bmatrix} C_{f11} & C_{f12} & C_{f13} & 0 \end{bmatrix} (\mathrm{i}\omega) + \begin{bmatrix} K_{f11} & K_{f12} & K_{f13} & K_{f14} \end{bmatrix} \right) \begin{Bmatrix} \{\boldsymbol{\Theta}\} \\ \{\boldsymbol{\eta}\} \\ \{\mathbf{q}(-1/2)\} \\ \{\mathbf{C}\} \end{Bmatrix}, \tag{26}$$

where $[J_{fij}]$, $[C_{fij}]$ and $[K_{fij}]$ are $n \times n$ matrices, and the elements of each matrix are constants or functions of the flow resistance $\lambda l/\bar{h}$. Additionally, The vectors $\{\mathbf{f_z}\}, \{\boldsymbol{\Theta}\}, \{\boldsymbol{\eta}\}, \{\mathbf{q}(-1/2)\}$ and $\{\mathbf{C}\}$ denote the fluid force vector, rotation angle vector, parallel displacement vector, fluctuating flow vector and integration constant vector, respectively, and are expressed as

$$\{\mathbf{f_z}\} = \begin{Bmatrix} f_{z1} & f_{z2} & \cdots & f_{zn} \end{Bmatrix}, \{\boldsymbol{\Theta}\} = \begin{Bmatrix} \Theta_1 & \Theta_2 & \cdots & \Theta_n \end{Bmatrix}, \{\boldsymbol{\eta}\} = \begin{Bmatrix} \eta_1 & \eta_2 & \cdots & \eta_n \end{Bmatrix},$$
$$\{\mathbf{q}(-1/2)\} = \begin{Bmatrix} q_1(-1/2) & q_2(-1/2) & \cdots & q_n(-1/2) \end{Bmatrix}, \{\mathbf{C}\} = \begin{Bmatrix} C_1 & C_2 & \cdots & C_n \end{Bmatrix}$$

It can easily be seen from Eq. (26) that the nondimensional fluid force vector $\{f_z\}$ is composed of the components proportional to $(\mathrm{i}\omega)^2$, $(\mathrm{i}\omega)^1$ and $(\mathrm{i}\omega)^0$.

3.5. Boundary conditions at the end of each sheet element

Because the pressure and flow rate must be continuous between element i and element $i+1$, the following equations should be satisfied:

$$p_{i-1}(1/2) = p_i(-1/2) \quad (i = 2, 3, \cdots, n), \tag{27}$$

$$q_{i-1}(1/2) = q_i(-1/2) \quad (i = 2, 3, \cdots, n). \tag{28}$$

Here, special attention must be paid to the boundary conditions at the inlet of element 1 and the outlet of element n, where boundary conditions (18) and (19) are applied.

3.6. Relationship between the amplitude $\{\boldsymbol{\eta}\}$ of translational vibration and amplitude $\{\boldsymbol{\Theta}\}$ of rotational vibration

According to Eq. (14), the displacement of center point c of element i in z-direction is expressed by $\Delta h_i \mathrm{e}^{\mathrm{i}\Omega t}$, as shown in Fig. 8. Moreover, under the assumption that ϕ_i is small, the following approximation holds:

$$\Delta h_i^{\Omega t} = \sum_{j=1}^{i-1} l_j \sin\phi_j + \frac{1}{2} l_i \sin\phi_i \approx \sum_{j=1}^{i-1} l_j \phi_j + \frac{1}{2} l_i \phi_i = \sum_{j=1}^{i-1} l_j \Delta\theta_{0j}^{\Omega t} + \frac{1}{2} l_i \Delta\theta_{0i}^{\Omega t}. \tag{29}$$

After nondimensionalization we obtain

$$\eta_i = \Delta h_i/\bar{h} = \sum_{j=1}^{i-1} \Theta_j + \frac{1}{2}\Theta_i. \tag{30}$$

The above relationship can easily be rewritten into the following matrix form:

$$\{\boldsymbol{\eta}\} = \begin{bmatrix} T_\eta & 0 \end{bmatrix} \begin{Bmatrix} \{\boldsymbol{\Theta}\} \\ \{\mathbf{q}(-1/2)\} \end{Bmatrix}, \tag{31}$$

where $[T_\eta]$ is an $n \times n$ matrix the elements of which are constants (refer to Appendix A). Besides, vector $\{\mathbf{q}(-1/2)\}$ is added into Eq. (31) for later transformation.

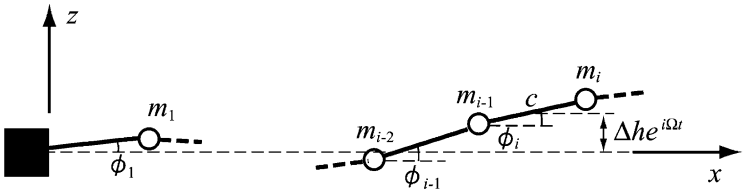

Fig. 8. Relationship between $\{\boldsymbol{\eta}\}$ and $\{\mathbf{T}\}$.

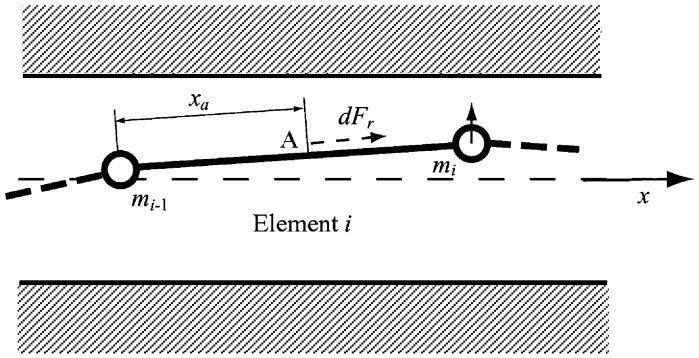

Fig. 9. Frictional forces acting on the surface of the elements.

3.7. Formulation of the fluid frictional force

When the flow is regarded as a 2-D Poiseuille flow, the shearing stress due to the steady flow component may be calculated by

$$\tau = 6\mu\bar{Q}/\bar{h}^2. \tag{32}$$

As shown in Fig. 9, the fluid frictional force dF_r acting at point A of element i in the x_a direction can be expressed as

$$\mathrm{d}F_r = 2\tau\,\mathrm{d}x_a. \tag{33}$$

Integrating the frictional force over the surface of each sheet element with respect to x_a, we can obtain $F_r = 2\tau l$. After that, we transform all frictional forces acting on the surfaces F_r to generalized forces and express them as a function of $\{\boldsymbol{\varphi}\}$ in vector form as follows:

$$\{\mathbf{Q_r}\} = 2\tau l^2[L_2]\{\boldsymbol{\phi}\}, \tag{34}$$

where $\{\mathbf{Q_r}\}$ and $\{\boldsymbol{\phi}\}$ denote the frictional moment vector and the rotational angle vector, respectively, and $[L_2]$ is a $n \times n$ matrix the elements of which are constants (refer to Appendix A). Furthermore, substituting Eq. (34) into Eq. (9), the equation of motion becomes

$$[J_M]\{\ddot{\boldsymbol{\phi}}\} + [C_M]\{\dot{\boldsymbol{\phi}}\} + \left([K_M] - 2\tau l^2[L_2]\right)\{\boldsymbol{\phi}\} = \{\mathbf{Q_z}\} \tag{35}$$

From Eq. (35), it can be seen that the frictional force influences the stiffness of the system.

3.8. Expansion of the equation of motion

Combining Eqs. (26) and (31) with boundary condition Eqs. (18), (19), (27) and (28), a $4n \times 4n$ expression of nondimensional fluid force vector $\{\mathbf{f_z}\}$ acting on mass particles in the z direction may be expressed, using as variables the amplitude of the rotation angle $\{\boldsymbol{\Theta}\}$ and the fluctuating flow rate at the inlet of each element $\{\mathbf{q}(-1/2)\}$ in nondimensional form. Furthermore, after transforming the nondimensional fluid force vector $\{\mathbf{f_z}\}$ into a dimensional

vector, the generalized dimensional fluid moment vector $\{\mathbf{Q_z}\}$ corresponding to $\{\mathbf{f_z}\}$ is obtained as

$$\{\mathbf{Q_z}\} = \rho \frac{\bar{Q}^2}{\bar{h}^2} l e^{\Omega t}[L_3]\{\mathbf{f}_z\}, \tag{36}$$

where $[L_3]$ is a $n \times n$ matrix, the elements of which are constant (refer to Appendix A).

In Eq. (35), the following transformation $\{\boldsymbol{\phi}\} = \{\boldsymbol{\Delta\theta_0}\}^{\Omega t} = \bar{h}\{\boldsymbol{\Theta}\}^{\Omega t}/l$ is effected for computing the eigenvalues of Eq. (35). Moreover, introducing a new variable defined by $\{\boldsymbol{\kappa}\} = (\omega)\{\boldsymbol{\Theta}\}$, the characteristic equation for Eq. (35) may be expressed as

$$([M_a](\mathrm{i}\omega) - [K_a]) \begin{Bmatrix} \{\boldsymbol{\kappa}\} \\ \{\boldsymbol{\Theta}\} \\ \{\mathbf{q}(-1/2)\} \end{Bmatrix} = 0, \tag{37}$$

where $[M_a]$ and $[K_a]$ are both $3n \times 3n$ matrices, the elements of which are constants and not a function of frequency ω. Therefore, the eigenvalue can be computed directly from Eq. (37) without iteration.

On the contrary, in the case of the method proposed by Kaneko et al. (2000), where the finite element method is employed for the stability analysis of sheet flutter, an iterative scheme was necessary for calculating the eigenvalues, because the frequency ω is included in the elements of the mass and stiffness matrices.

As expected, the proposed method contributed to the reduction of the calculation time greatly and would be a useful tool for the analysis of 3-D sheet flutter.

4. Nonlinear Analysis

In the previous section, a linear analysis was presented for predicting the critical flow speed and flutter frequency, where nonlinear terms in the expressions of the fluid dynamic forces were neglected. However, when the flow speed exceeds the critical flow speed, the amplitude of flutter grows with increasing flow speed. In these situations, the effect of nonlinear terms emerges. For elucidating the unsteady behavior of the sheet subjected to leakage flow beyond the critical flow speed, a nonlinear flutter analysis is performed here based on the model shown in Figs. 1 and 2.

The equation of motion for the sheet may be obtained in the same manner as used to derive Eq. (9), and the basic equation of leakage flow is applied in the nonlinear analysis as well. However, the derivation process for the nonlinear fluid dynamic forces is quite different from that for the linear ones, as discussed below.

4.1. Fluid forces acting on elements from inflow in the lower passage

In this section, attention is paid to the flow between the ith element and the lower wall of the passage, shown in Fig. 10. In this figure, the positive direction of the x-axis is defined as pointing to the right along the central line of the leakage flow, and upwards from the center point of the element c is defined as the positive direction of the z-axis. Therefore, the distance from the lower wall to the element may be described as a function of distance from lower wall to center point c, noted as h_c, and the rotational angle of the element ϕ_i:

$$h_i^L(x,t) = h_{ci}(t) + x\tan\phi_i(t), \tag{38}$$

where L and i denote the lower passage and the ith element, respectively.

Eqs. (10) and (11) are applied to the flow under ith element. By substituting Eq. (38) into Eq. (10) and integrating it with respect to x, the flow rate may be obtained as

$$Q_i^L(x,t) = -\dot{h}_{ci}x - \frac{x^2}{2}\dot{\phi}_i\sec^2\phi_i + C_{Qi}^L(t) \quad (i = 1,2,\cdots,n), \tag{39}$$

where $C_{Qi}^L(t)$ is an integration constant which is a function of time t.

By substituting Eqs. (38) and (39) into Eq. (11), the pressure gradient becomes

$$\frac{\partial P_i^L(x,t)}{\partial x} = W_i^L(x,t) - \frac{\rho}{h_i^L}\dot{C}_{Qi}^L(t) \quad (i = 1,2,\cdots,n), \tag{40}$$

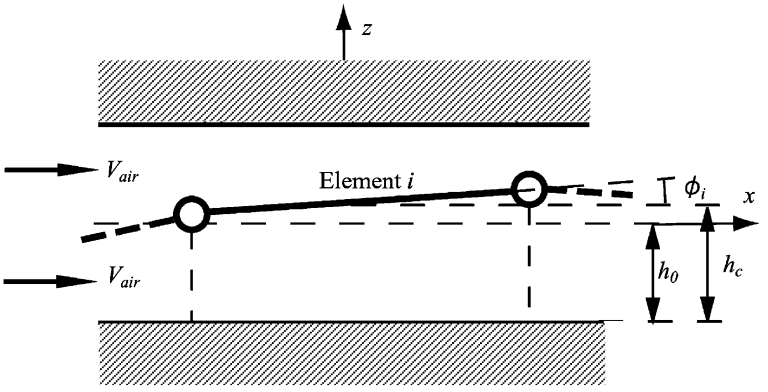

Fig. 10. Motion of an element in nonlinear analysis.

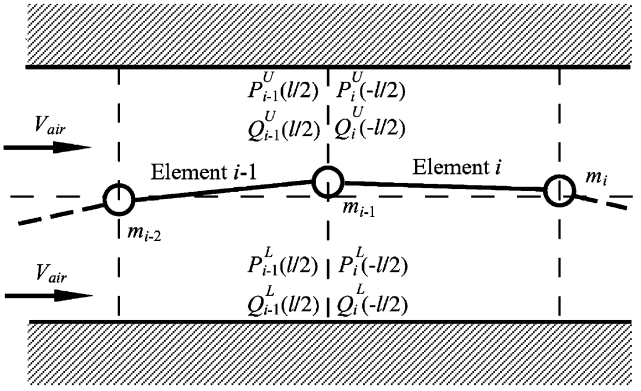

Fig. 11. Continuity conditions between two elements.

where

$$W_i^L(x,t)=\frac{\rho\ddot{h}_{ci}}{h_i^L}x+\frac{\rho}{2h_i^L}x^2\ddot{\phi}_i\sec^2\phi_i+\frac{\rho}{h_i^L}x^2\dot{\phi}_i\tan\phi_i\sec^2\phi_i+\frac{2\rho Q_i^L\dot{h}_{ci}}{h_i^{L^2}}+\frac{2\rho Q_i^L}{h_i^{L^2}}x\dot{\phi}_i\sec^2\phi_i+\frac{\rho Q_i^{L^2}}{h_i^{L^3}}\tan\phi_i-\frac{\lambda\rho}{4h_i^{L^3}}Q_i^L|Q_i^L|. \tag{41}$$

Based on the above, it can be seen that the pressure gradient in the x-direction can be expressed as a nonlinear function of the acceleration, velocity and displacement of the center point c, the flow rate, and the rotational acceleration, rotational velocity and rotational displacement of the element.

4.2. Boundary conditions

As shown in Fig. 11, the pressure and flow rates must be continuous between element i and element $i+1$, resulting in the following equations:

$$P_{i-L}^L(l/2,t)=P_i^L(-l/2,t)\quad(i=2,3,\cdots,n), \tag{42}$$

$$Q_{i-L}^L(l/2,t)=Q_i^L(-l/2,t)\quad(i=2,3,\cdots,n), \tag{43}$$

Furthermore, the boundary conditions at the left and right ends of the lower flow passage shown in Fig. 1 may be written in the same form as Eqs. (12) and (13):

$$P_1^L\left(-\frac{l}{2}\right)=P_a-\xi_a^L\frac{\rho}{2}\frac{Q_1^L\left(-\frac{l}{2},t\right)^2}{h_1^L\left(-\frac{l}{2},t\right)^2}\quad\text{and}\quad P_n^L\left(\frac{l}{2}\right)=P_b-\xi_b^L\frac{\rho}{2}\frac{Q_n^L\left(\frac{l}{2},t\right)^2}{h_n^L\left(\frac{l}{2},t\right)^2}, \tag{44,45}$$

where ξ_a^L and ξ_b^L are pressure-loss coefficients in area A and area B of Fig. 1, respectively. It is assumed that pressure in area A is higher than in area B throughout the computation, but reverse flow possibly occurs in areas A and B due to the large deformation of the sheet. Therefore, the values of ξ_a^L and ξ_b^L are determined by the direction of flow:
(i) when $Q_1^L(-l/2)<0$ (A is outlet), $\xi_a^L=\xi_{ex}$; (ii) when $Q_1^L(-l/2)\geq 0$ (A is inlet), $\xi_a^L=\xi_{in}$;
(iii) when $Q_1^L(l/2)\leq 0$ (B is inlet), $\xi_b^L=\xi_{in}$; (iv) when $Q_1^L(l/2)>0$ (B is outlet), $\xi_b^L=\xi_{ex}$.

4.3. Formulation of the integration constant

From Eq. (42) for the pressure in the lower flow passage , it can be found that the difference between the pressure right after inlet $P_n^L(l/2,t)$ and the pressure just before outlet $P_1^L(-l/2,t)$ is the sum of the pressure loss in all the elements,

$$\sum_{i=1}^{n}\int_{-1/2}^{1/2}\frac{\partial P_i^L(x,t)}{\partial x}\,\mathrm{d}x=P_n^L\left(\frac{l}{2},t\right)-P_1^L\left(-\frac{l}{2},t\right). \tag{46}$$

Substituting Eq. (40) into Eq. (46), we can obtain

$$\sum_{i=1}^{n}\left(\dot{C}_{Qi}^L(t)\int_{-l/2}^{l/2}\frac{\rho}{h_i}\,\mathrm{d}x\right)=\sum_{t=1}^{n}\left(\int_{-l/2}^{l/2}W_i^L(x,t)\,\mathrm{d}x\right)+P_1^L\left(-\frac{l}{2}\right)-P_n^L\left(\frac{l}{2}\right). \tag{47}$$

In addition, differentiating Eq. (39) and Eq. (43) with respect to time yields

$$\frac{\partial Q_i^L(x,t)}{\partial t}=U_i^L(x,t)+\dot{C}_{Qi}^L(t), \tag{48}$$

$$\frac{\partial Q_{i-1}^L(l/2,t)}{\partial t}=\frac{\partial Q_i^L(-l/2,t)}{\partial t}\quad(i=2,3,\cdots,n). \tag{49}$$

where

$$U_i^L(x,t)=-\ddot{h}_{ci}x-\frac{x^2}{2}\ddot{\phi}_i\sec^2\phi_i-x^2\dot{\phi}_i^2\sec^2\phi_i\tan\phi_i$$

Substituting Eq. (48) into Eq. (49) yields

$$U_{i-1}^L\left(\frac{l}{2},t\right)+\dot{C}_{Qi-1}^L(t)=U_i^L\left(-\frac{l}{2},t\right)+\dot{C}_{Qi}^L(t)\quad(i=2,3,\cdots,n). \tag{50}$$

Expressing Eq. (47) and Eq. (50) in matrix form, we obtain

$$[A_1]\left\{\dot{\mathbf{C}}_Q^L(t)\right\}=\{A_2\}, \tag{51}$$

where $[A_1]$ is a $n\times n$ matrix, $\{A_2\}$ is a $1\times n$ vector (refer to Appendix A), and $\left\{\dot{\mathbf{C}}_Q^L(t)\right\}=\left\{\begin{array}{cccc}\dot{C}_{Q1}^L(t) & \dot{C}_{Q2}^L(t) & \cdots & \dot{C}_{Qn}^L(t)\end{array}\right\}^{\mathrm{T}}$. Integration terms appearing in the matrix $[A_1]$ and the vector $\{A_2\}$ can be computed using numerical integration.

The pressure right after inlet $P_1^L(-l/2)$ and just before outlet $P_n^L(l/2)$ can be computed by means of Eqs. (44) and (45). From Eq. (51) the formulation of $\left\{\dot{\mathbf{C}}_Q^L(t)\right\}$ may be given by

$$\left\{\dot{\mathbf{C}}_Q^L(t)\right\}=[A_1]^{-1}\{A_2\}. \tag{52}$$

4.4. Calculation of the fluid forces

Under the conditions of pressure continuity, it can be seen that the pressure distribution on the ith sheet, influenced by the lower flow, is the sum of pressure right after inlet, the pressure difference from the 1st element to the (i-1)th element, and the pressure difference from the inlet of the ith element to x, i.e.,

$$P_i^L(x,t)=P_1^L\left(-\frac{l}{2},t\right)+\sum_{j=1}^{i-1}\int_{-1/2}^{x}\frac{\partial P_j^L(x,t)}{\partial x}\,\mathrm{d}x+\int_{-1/2}^{x}\frac{\partial P_i^L(x,t)}{\partial x}\,\mathrm{d}x. \tag{53}$$

Rewriting the above equation in matrix form results in

$$\left\{P_1^L(x,t)P_2^L(x,t)\cdots P_n^L(x,t)\right\}^{\mathrm{T}} = [A_3]\left\{P_1^L\left(-\frac{l}{2},t\right)\int_{-l/2}^{l/2}\frac{\partial P_1^L(x,t)}{\partial x}\,\mathrm{d}x\cdots\int_{-l/2}^{l/2}\frac{\partial P_{n-1}^L(x,t)}{\partial x}\int_{-l/2}^{l/2}\frac{\partial P_{n-1}^L(x,t)}{\partial x}\right\}^{\mathrm{T}} + \left\{\int_{-l/2}^{x}\frac{\partial P_1^L(x,t)}{\partial x}\,\mathrm{d}x\int_{-l/2}^{x}\frac{\partial P_2^L(x,t)}{\partial x}\,\mathrm{d}x\cdots\int_{-l/2}^{x}\frac{\partial P_n^L(x,t)}{\partial x}\,\mathrm{d}x\right\}^{\mathrm{T}}, \tag{54}$$

where $[A_3]$ is a $n\times n$ matrix (refer to Appendix A).

The procedure for the formulation from pressure to fluid forces is similar to that which was used in the linear analysis in Eq. (25) in Section 4.4. In this case, we can obtain a similar equation describing dimensional fluid forces per unit width acting on all mass particles, namely

$$\left\{\mathbf{F}^L\right\} = \frac{1}{l}\int_{-l/2}^{l/2}\left\{\mathbf{P}^L(x,t)\right\}\left(\frac{l}{2}+x\right)\mathrm{d}x + \frac{1}{l}[L_1]\int_{-l/2}^{l/2}\left\{\mathbf{P}^L(x,t)\right\}\left(\frac{l}{2}-x\right)\mathrm{d}x, \tag{55}$$

where

$$\left\{\mathbf{F}^L\right\} = \left\{F_1^L \quad F_2^L \quad \cdots \quad F_n^L\right\}^{\mathrm{T}}, \quad \left\{\mathbf{P}^L(x,t)\right\} = \left\{P_1^L(x,t) \quad P_2^L(x,t) \quad \cdots \quad P_n^L(x,t)\right\}^{\mathrm{T}}.$$

In addition, the upper flow contribution to the fluid force vector can be formulated in the same way:

$$\left\{\mathbf{F}^U\right\} = \left\{F_1^U \quad F_2^U \quad \cdots \quad F_n^U\right\}^{\mathrm{T}}.$$

Last, from the Lagrange equation,

$$Q_{zj} = \sum_i F_i\cdot\frac{\partial z_i}{\partial \phi_j},$$

and we can calculate the generalized force $\{\mathbf{Q}_z\}$ as

$$\left\{\mathbf{Q_z}\right\} = [A_4]\left(\left[\mathbf{F}^L\right] - \left[\mathbf{F}^U\right]\right), \tag{56}$$

where $[A_4]$ is a $n\times n$ matrix (refer to Appendix A).

4.5. Calculation procedure

Coupling Eqs. (35), (39), (40), (44), (45), (52), and (54)–(56), the state of the system at time $t = t_0 + \Delta t$ may be calculated by numerical integration if the state of the system at time $t = t_0$ is known. Here, the Newmark-β method is applied in the computation, and trapezoid integration is used in the numerical integration appearing in Eqs. (52), (54) and (55).

5. Comparison of linear and nonlinear methods in the case of forced vibration

Both linear and nonlinear analyses of the fluid forces were performed in the foregoing. In the linear analysis, the second- and higher-order terms in the basic equations of leakage flow and boundary conditions are neglected in the course of the derivation of the fluid force, and the coupled fluid–structure motion equations result in an eigenvalue problem. On the other hand, in the nonlinear analysis, the basic equations of leakage flow are transformed to ordinary differential equations by means of discretization of the sheet, and the time-history response of the system is computed using numerical computation. As an example, when the upper wall shown in Fig. 5 vibrates translationally around the equilibrium height $\bar{h}$ with angular frequency Ω, and simultaneously vibrates rotationally around the central point c of upper wall with the same angular frequency, we compute the force and moment acting on the upper wall with changing vibration amplitude via both linear and nonlinear analyses. In this computation we assign a phase lag 60° between translational and rotational vibrations.

For small vibration amplitudes, the results of the two methods of calculation are presented in Fig. 12. Both results show highly similar curves, indicating the correctness of the linear approach. However, in the case of large vibrations as plotted in Fig. 13, with the emergence of nonlinear effects in the fluid pressure, the actual fluid force and moment become disparate, showing that nonlinear effects in the fluid pressure calculation cannot be ignored. The nonlinear terms appearing here are considered to be the main factor causing limit-cycle vibration, which is discussed later.

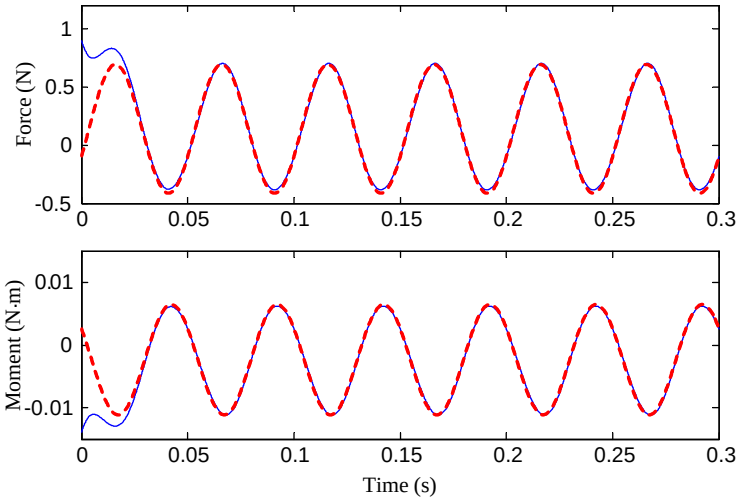

Fig. 12. Comparison of forces and moments obtained by linear and nonlinear methods (small amplitude):——, results of nonlinear calculation; – –, results of linear calculation.

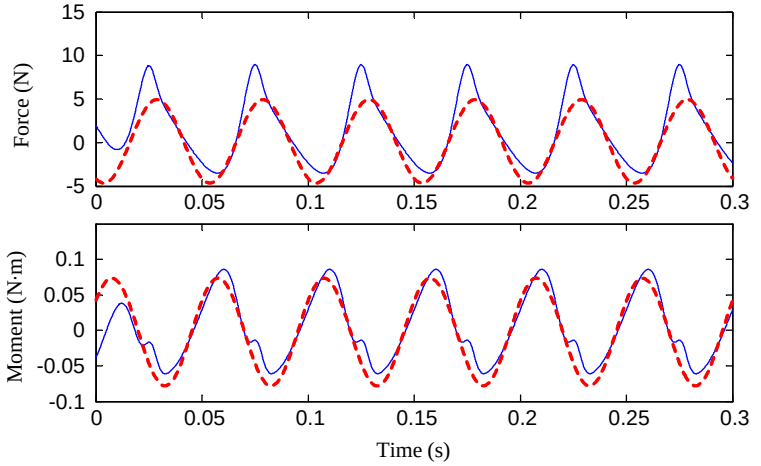

Fig. 13. Comparison of forces and moments obtained by linear and nonlinear methods (large amplitude): ——, results of nonlinear calculation; – –, results of linear calculation.

6. Calculation example

6.1. Linear analysis

In this section, we perform a linear stability analyses for a cantilever beam subjected to leakage flow using the proposed method.

For these calculations, the experimental parameters and results contributed by Nagakura and Kaneko (1992) are used to make a comparison between calculated and experimental results. Fig. 14 shows the experimental set-up wherein a thin elastic plate made of bronze is fixed with one end while the other end is free. Air-flows through two leakage passages composed of the sidewalls and the elastic plate. The parameters of the experimental set-up and test conditions are summarized in Table 1.

Complex eigenvalues corresponding to Nagakura and Kaneko's experiments were calculated from Eq. (37). A positive real eigenvalue denotes flutter, indicating that the vibration amplitude of the plate increases with time. In this calculation, we chose 20 as the number of plate segments.

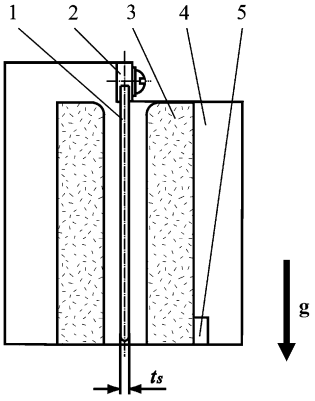

Fig. 14. Test section. 1: elastic plate; 2: support; 3: wall of passage; 4: side wall of passage; 5: photonic sensor.

Table 1
Test conditions in Nagakura and Kaneko's paper

Material	Bronze sheet
Thickness t_s (m)	2×10^{-4}
Young's modulus E (Pa)	1.10×10^{11}
Density ρ (kg/m^3)	8.78×10^3
Length of passage L (m)	0.20
Width of passage b (m)	0.10
Height of passage h_0 (m)	Varies from 0.8×10^{-3} to 9.0×10^{-3}
Viscosity of fuild μ (Pa s)	1.8×10^{-5}

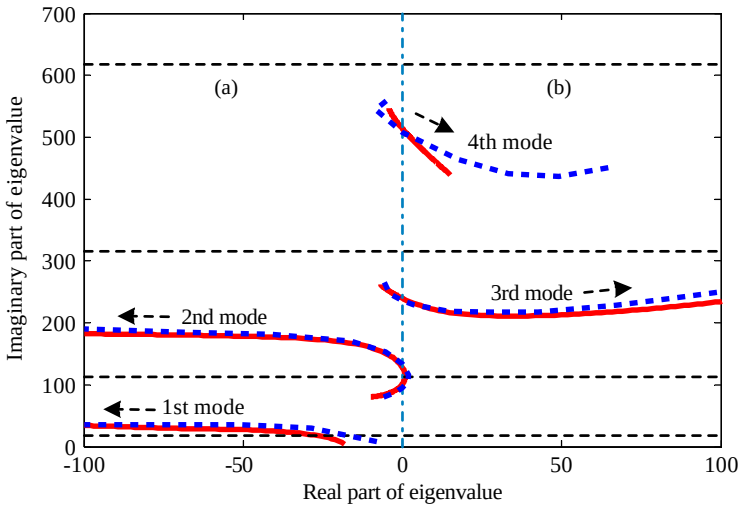

Fig. 15. Root loci of characteristic equation ($h_0 = 2.5$ mm) ; x axis: the real part of eigenvalue; y axis: the imaginary part of eigenvalue; (a) stable area; (b) unstable area; ▬, results by proposed method; ▪▪▪, results by modal analysis; ▬ ▬, results without fluid effect; ▬ ▪, line splitting stable area and unstable area.

The root loci of the characteristic equation are plotted in Fig. 15. Solid lines for increasing oncoming air-flow velocity in the case of an average passage height h_0 of 2.5 mm.The horizontal axis indicates the damping ratio and the vertical axis indicates the angular vibration frequency. Increasing oncoming flow velocity is indicated by arrows in the figure,

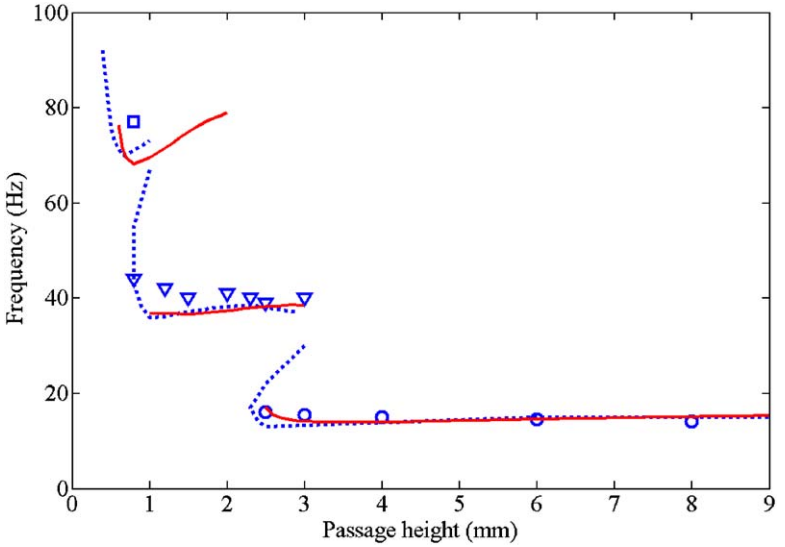

Fig. 16. Passage height versus flutter frequency: □, experiments (2nd mode); ▽, experiments (3rd mode); ○, experiments (4th mode); ▪▪▪▪, linear calculation results by modal analysis; ▬, linear calculation results by proposed method.

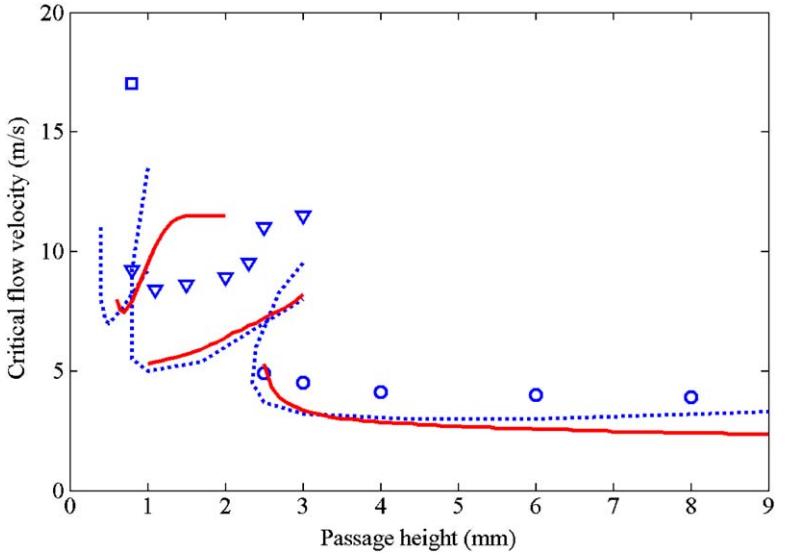

Fig. 17. Passage height versus critical flow velocity: □, experiments (2nd mode); ▽, experiments (3rd mode); ○, experiments (4th mode); ▪▪▪▪, linear calculation results by modal analysis; ▬, linear calculation results by proposed method.

and the broken lines correspond to the 1st to 4th angular vibration frequencies of the system with zero fluid forces. The calculation results by modal analysis are plotted with dotted lines, which are compared with the results from the proposed method (solid line). From the figure we see that the real part of the 2nd mode eigenvalue becomes positive at a certain flow velocity, denoting flutter. When the flow velocity increases, it returns to stability, followed by 3rd mode flutter at a higher flow velocity. The experimental and computational results by Nagakura and Kaneko (1992) illustrate the same phenomena.

In Figs. 16 and 17, the critical flow speeds and flutter frequencies computed by the proposed method are plotted against the passage height, and they are compared with the experimental and computational results by Nagakura and Kaneko (1992). A good agreement between the calculated and experimental results is obtained, and all the results

demonstrate that both the critical flow speeds and the flutter frequencies vary step-wise when the passage height h_0 increases continuously. It should be noted that, because the proposed calculation is based on the assumption that the structural damping for the cantilever plate is zero, the computed critical flow speeds are lower than those of Nagakura and Kaneko's experimental results when the passage height increases.

In the experimental study of sheet flutter by Watanabe et al. (2002a), a nondimensional critical flow velocity V^*_{crit} was introduced based on the experimentally founded relationship between the critical flow velocity V_{crit}, bending stiffness per unit width EI, and length of the sheet L, as shown below

$$V^*_{\text{crit}} = V_{\text{crit}} \Big/ (EI/\rho L^3)^{1/2}.$$

The solution of V^*_{crit} against mass ratio μ_m is shown in Fig. 18. The dashed and dotted lines indicate the theoretical results of Watanabe et al. (2002b) for drag coefficient $C_D = 0$ and 0.2, respectively, and the results of a potential flow analysis by Huang (1995) are plotted with a thick line for high μ_m. Experimental results quoted from Watanabe et al. (2002b), Huang (1995) and Kornecki et al. (1976) are included in the graph as well. For comparison we employ the proposed method to calculate V^*_{crit}, the solution of which is plotted as a solid line. From the figure we see that all the results show a decrease in V^*_{crit} when μ_m increases, and the computation results from the proposed method agree well with the experimental results over a wide range, especially near $\mu_m = 1$.

6.2. Nonlinear analysis

In this section, the nonlinear analysis is used to investigate the behavior of a cantilever sheet subjected to leakage flow using the proposed method. The test conditions are presented in Table 2, corresponding to a mass ratio of 5.49. The time response of the sheet is calculated by changing the average velocity of air flowing through the leakage passages. In this computation, we chose 10 segments of the sheet.

Fig. 19 shows the calculated results of the response time-history of the sheet when a small disturbance is initially employed for a given flow velocity. When the average flow velocity V_{air} is small, the vibration amplitude of the sheet deceases with time, indicating that the system is stable, as shown in Fig. 19(a). It can be found that fluid damping is positive in this case since the structural damping is assumed to be zero in the calculation. Increasing the average flow velocity to a critical flow velocity of 11.4 m/s, Fig. 19(b) (we call the threshold velocity between the stable area and the limit-cycle area the critical flow velocity), we find that the sheet vibrates continually with a certain amplitude that depends on the initial conditions. When the average flow velocity exceeds the critical flow, a small initial disturbance leads to increasing vibration amplitude of the sheet as shown in Fig. 19(c). This figure shows that the amplitude of the sheet increases with time, and after a certain period of growth, steady vibration continues with a certain vibration amplitude, that is limit-cycle vibration arises. At this point in time, the vibration amplitude of the sheet is of the same order as the leakage passage height, and the motion is nonharmonic. As shown in Fig. 19(d), if the flow velocity increases further and exceeds the upper boundary of 17.8 m/s (we call the velocity separating the limit-cycle region from the unstable region the unstable flow velocity), the amplitude of limit-cycle vibration increases until the sheet collides with a side wall, causing chaotic behavior. Because the collision conditions are not taken into account in this model, the calculation was stopped at the instant when the sheet collides with the side wall. In Fig. 19 only the time responses of the nth element are presented, but other elements show similar behavior as well.

A stability chart is obtained as a summary of the analyses, in Fig. 20. The state of the system may be classified as stable, limit-cycle motion, and unstable, depending on the flow velocity. Additionally, the rotational vibration amplitude of the first element ϕ_1 and that of nth element ϕ_n are plotted against flow velocity in Fig. 20 when the sheet is in a limit-cycle state. It can be seen that vibration amplitudes of sheet elements increase with flow velocity under limit-cycle conditions.

Fig. 21 presents the mode shape of sheet corresponding to different flow velocities in limit-cycle conditions. From the figure, it is seen that all waves are travelling waves. Furthermore, the behavior of the sheet becomes complicated as a result of higher-order mode contributions when the flow velocity increases.

Fig. 22 shows the corresponding spectral content of the vibration in FFT diagrams. Fig. 22(a) shows that the sheet vibrates with a single frequency in the case of $V_{\text{air}} = 11.4$ m/s (critical flow velocity). However, increasing flow velocity brings about the emergence of higher-order frequency components, which grow with flow velocity. Figs. 22(b) and 22(c) show the case of $V_{\text{air}} = 14.1$ m/s and $V_{\text{air}} = 17.3$ m/s, respectively.

Fig. 23 illustrates the relationship between the dominant frequency of sheet vibration and flow velocity. It can be seen that the dominant frequency increases with flow velocity and the stiffness of the system increases under the influence of flow as well. From Section 4.7 we know that fluid frictional force influences the stiffness of the system. As shown in Eqs. (32) and (35), the shearing force τ and the stiffness increase with flow velocity. As a result, tension on the sheet

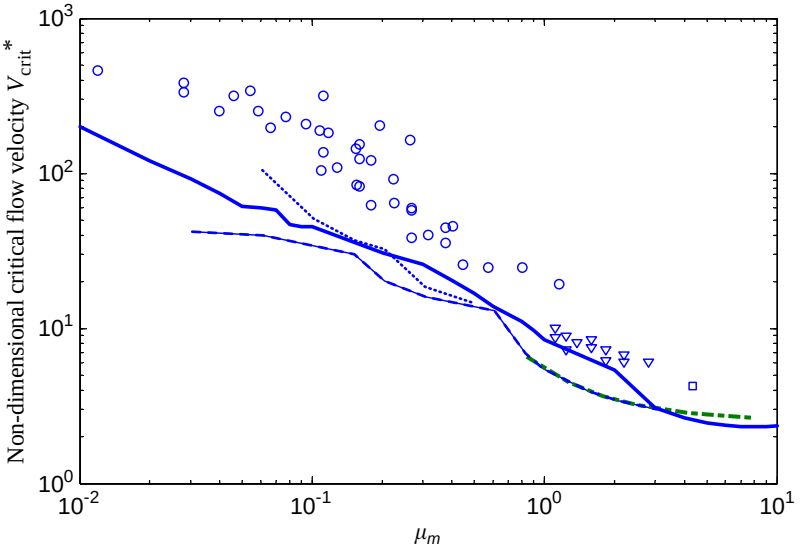

Fig. 18. Nondimensional critical flow velocity V^*_{crit} versus mass ratio μ_m: ○, experiments by Watanabe et al. (2002); ▽, experiments by Huang (1995); □, experiments by Kornecki et al. (1976); ▬ ▬, theory by Watanabe et al. where $C_D = 0$, (2002*a*, *b*); ▪▪▪▪▪▪▪, theory by Watanabe et al. where $C_D = 0.2$, (2002*a*, *b*); ▬ ▬ ▬, theory by Huang (1995); ▬, proposed theory

Table 2
Calculation parameters in the nonlinear analysis

Length of each element l (m)	0.02
Partition number	10
Height of passage $\bar{h}$ (m)	2.0×10^{-3}
Fluid	Air
m_i (kg)	2.63×10^{-2}
c_i (N s m)	0
k_i (N m)	1.55

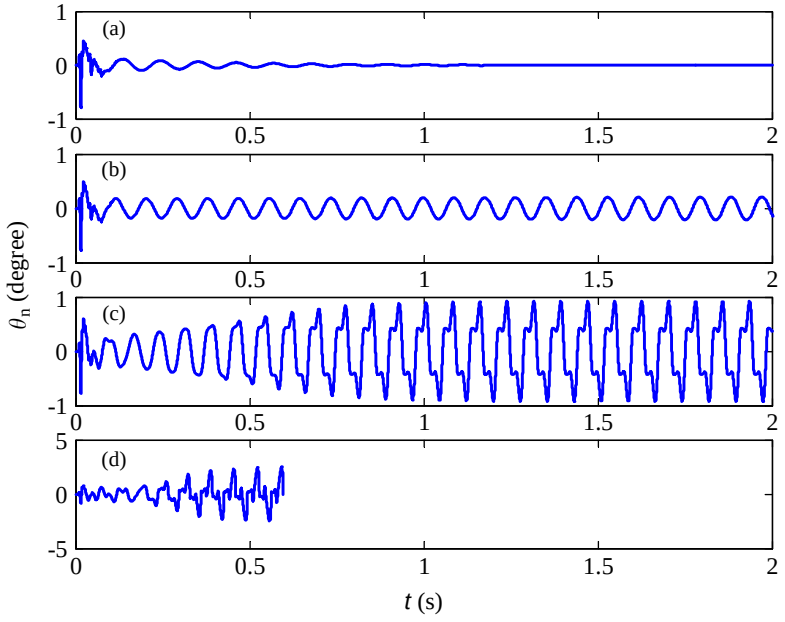

Fig. 19. Time history response of nth element of sheet: (a) $V_{\text{air}} = 9.13$m/s; (b) $V_{\text{air}} = 11.4$m/s; (c) $V_{\text{air}} = 14.1$m/s; (d) $V_{\text{air}} = 18.3$m/s.

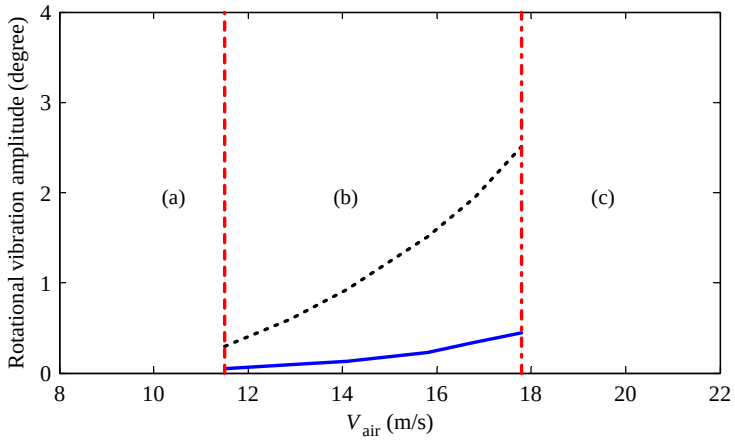

Fig. 20. Stability chart in passage height of $h_0 = 2$ mm: (a) stable area; (b) limit-cycle area; (c) unstable area; ▬, 1st element; ▪▪▪▪▪▪▪▪, nth element; ▬ ▬, lower boundary; ▬ ▪ ▬, upper boundary.

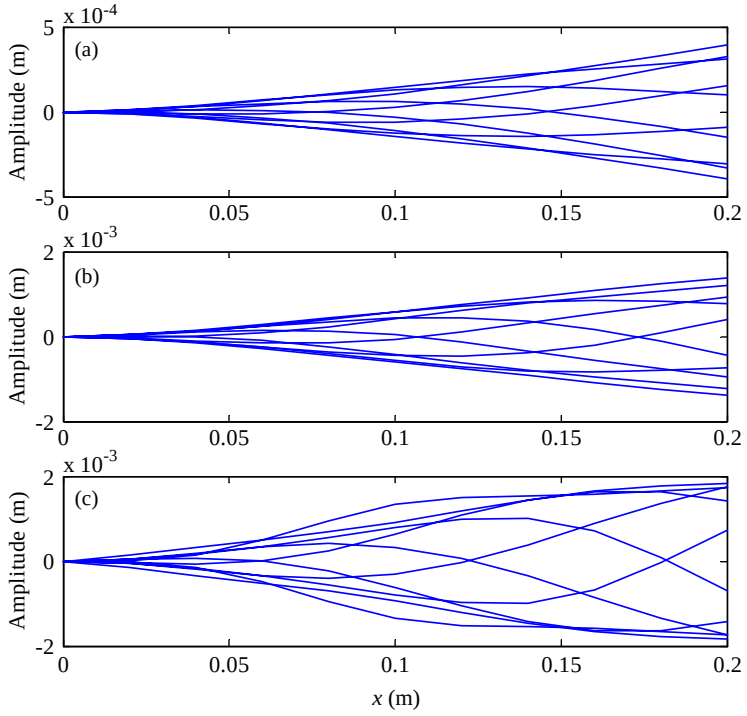

Fig. 21. Mode shape ($\mu_m = 5.49$, traveling wave): (a) $V_{air} = 11.4$m/s; (b) $V_{air} = 14.1$m/s; (c) $V_{air} = 17.3$m/s.

increases and raises the natural frequency of the sheet. The same tendency was indicated by Yamaguchi et al. (2003) as well.

Fig. 24 displays the stability chart in the case of an average passage height h_0 of 4 mm.As with the case of $h_0 = 2$ mm, the state of the system may be divided into stable, limit-cycle motion, and unstable areas depending on the flow velocity. Fig. 25 shows the calculated results of the critical flow velocity and unstable flow velocity by changing the height of the leakage passage. The area under the curve of critical flow velocity (solid line) is the stable, the area between the two curves (broken line) is the limit-cycle area, and the area over the broken line is the unstable area. It is shown that both critical flow velocity and unstable flow velocity decrease when the height of the leakage passage h_0 when h_0 is smaller

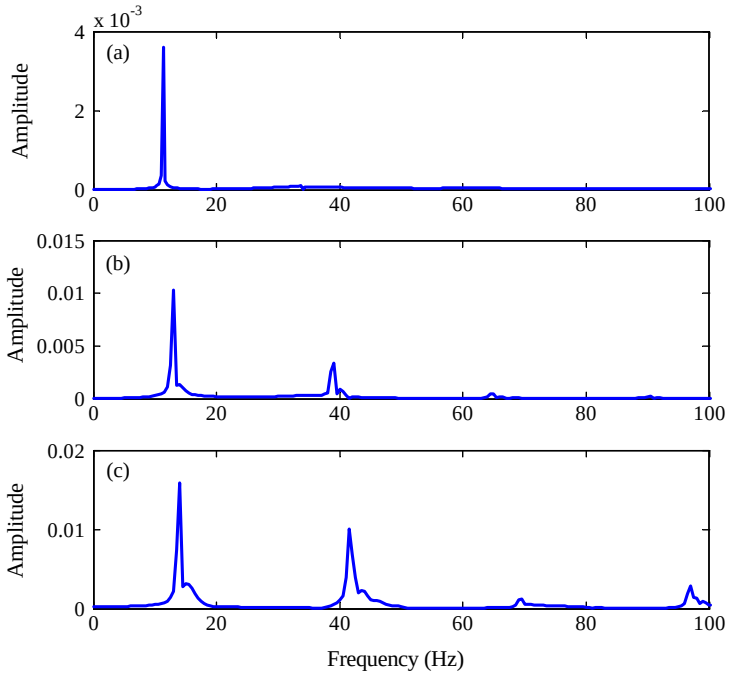

Fig. 22. Frequency spectrum vibration of nth element ($n = 10$): (a) $V_{air} = 11.4$m/s; (b) $V_{air} = 14.1$m/s; (c) $V_{air} = 17.3$m/s.

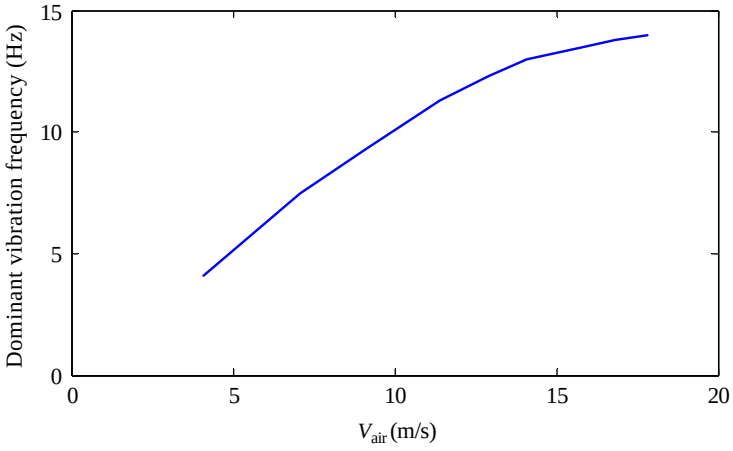

Fig. 23. Average flow velocity versus dominant vibration frequency.

than 2 mm.However, when h_0 becomes larger than 2 mm, we found that the values of the critical flow velocity and unstable flow velocity keep approximately constant, regardless of h_0.

7. Conclusion

In this paper, both linear and nonlinear analyses on a sheet-type structure under the effect of leakage flow were performed. It was shown that the proposed linear analysis adequately predicts the critical flow velocity of the sheet,

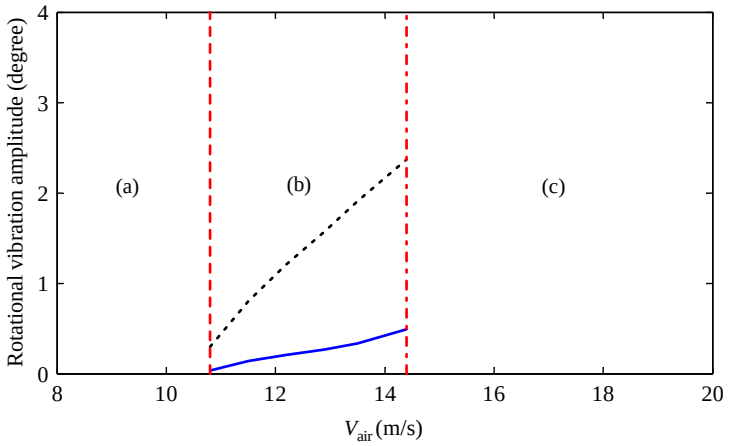

Fig. 24. Stability chart in passage heigth of $h_0 = 4$ mm: (a) stable area; (b) limit-cycle area; (c) unstable area; ▬, 1st element; ▪▪▪▪▪, nth element; ▬ ▬, lower boundary; ▬ ▪ ▬, upper boundary.

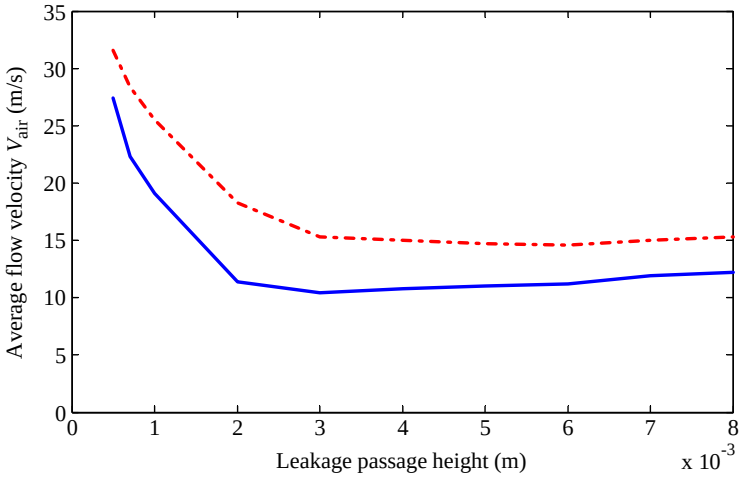

Fig. 25. Average flow velocity versus leakage passage height; ▬, Critical flow velocity; ▬ ▪ ▬, Unstable flow velocity.

achieving a good approximation, as seen by comparison with experiment. Solution was achieved by a noniteration method, with a dramatic decrease of calculation time as compared to the previously used iterative procedure.

In addition, it was found when the flow velocity exceeds the critical flow velocity, a nonlinear analysis of sheet behavior is needed, due to the large-amplitude vibration of the sheet. The nonlinear analysis demonstrated that the system shifts into limit-cycle and subsequently unstable conditions from a stable state, as the flow velocity is increased. We find that the dominant vibration frequency of the sheet increases with flow velocity, which cannot be observed in linear analysis.

Due to the fact that sheet materials of practical interest are variable and their damping is greatly variable, no structural damping was applied in both linear and nonlinear calculations. However, a loss factor can be taken into account easily in practical problems. In the future, it is expected that these solutions may be applied to predict the critical flow velocity, amplitude of limit-cycle vibration and unstable flow velocity in more complicated fluid structure coupling systems, with a large number of degrees of freedom, such as the flutter problems in production line of steel strips mentioned in the Introduction.

Appendix A

Some of the matrices used in the analysis are given below as

$$[L_1]=\begin{bmatrix}0 & 1 & & & 0\\ & 0 & 1 & & \\ & & \ddots & \ddots & \\ & & & & 1\\ 0 & & & & 0\end{bmatrix},\quad T_\eta=\begin{bmatrix}1/2 & & & & 0\\ 1 & 1/2 & & & \\ \vdots & \ddots & \ddots & & \\ 1 & \cdots & 1 & 1/2 & \end{bmatrix},\quad [L_2]=\begin{bmatrix}1-n & 1 & \cdots & 1\\ & 2-n & \ddots & \vdots\\ & & \ddots & 1\\ 0 & & & 0\end{bmatrix},\quad [L_3]=\begin{bmatrix}l_1 & & \cdots & & l_1\\ & l_2 & \cdots & & l_2\\ & \ddots & & & \vdots\\ & & l_i & \cdots & l_i\\ & & & \ddots & \vdots\\ 0 & & & & l_n\end{bmatrix}$$

$$[A_1]=\begin{bmatrix}-1 & 1 & 0 & \cdots & 0\\ 0 & -1 & 1 & & \vdots\\ \vdots & & \ddots & \ddots & 0\\ 0 & \cdots & 0 & -1 & 1\\ \int_{-l/2}^{l/2}\frac{\rho}{h_1^L}\,\mathrm{d}x & \int_{-l/2}^{l/2}\frac{\rho}{h_2^L}\,\mathrm{d}x & & \cdots & \int_{-l/2}^{l/2}\frac{\rho}{h_n^L}\,\mathrm{d}x\end{bmatrix},\quad \{A_2\}=\begin{Bmatrix}U_1^L\left(\frac{l}{2},t\right)-U_2^L\left(-\frac{l}{2},t\right)\\ U_2^L\left(\frac{l}{2},t\right)-U_3^L\left(-\frac{l}{2},t\right)\\ \vdots\\ U_{n-1}^L\left(\frac{l}{2},t\right)-U_n^L\left(-\frac{l}{2},t\right)\\ \sum_{i=1}^{n}\left(\int_{-l/2}^{l/2}W_i^L(x,t)\,\mathrm{d}x\right)+P_1^L\left(-\frac{l}{2}\right)-P_n^L\left(\frac{l}{2}\right)\end{Bmatrix},\quad [A_3]=\begin{bmatrix}1 & & 0\\ 1 & 1 & \\ \vdots & & \ddots\\ 1 & \cdots & 1\end{bmatrix},$$

$$[A_4]=l\begin{bmatrix}1 & \cdots & 1\\ & 1 & 1\\ & & \ddots & \vdots\\ 0 & & & 1\end{bmatrix}.$$

References

Antunes, J., 2002. Dynamics of rotor-flow coupled system. In: Anagonostopoulos, P. (Ed.), Flow-Induced Vibrations in Engineering Practice. WIT Press, Southampton, pp. 283–388.

Chang, Y.B., Moretti, P.M., 2000. Flow-induced vibration of free edges of thin films. In: Ziada, S., Staubli, T. (Eds.), Proceedings of Seventh International Conference on Flow-induced Vibrations. Balkema, Rotterdam, pp. 801–810.

Huang, L., 1995. Flutter of cantilevered plates in axial flow. Journal of Fluids and Structures 9, 127–147.

Inada, F., Hayama, S., 1987. A study on leakage-flow-induced vibrations (1st Report). Transactions of the Japan Society of Mechanical Engineers (in Japanese) 53C (488), 933–939.

Kaneko, S., Tanaka, S., Watanabe, T., 2000. Leakage flow induced flutter of highly flexible structures. In: Ziada, S., Staubli, T. (Eds.), Proceedings of Seventh International Conference on Flow-induced Vibrations. Balkema, Rotterdam, pp. 811–818.

Kornecki, A., Dowell, E.H., O'Brien, J., 1976. On the aeroelastic stability of two-dimensional panels in uniform incompressible flow. Journal of Sound and Vibration 47, 163–178.

Nagakura, H., Kaneko, S., 1992. The stability of a cantilever beam subjected to one-dimensional leakage flow. Transactions of the Japan Society of Mechanical Engineers (in Japanese) 58C (546), 352–359.

Nakashima, M., Utsumi, Y., Ono, K., 1999. Numerical simulation of motion of paper in three-dimensional air flow, Preprint. Japan Society of Mechanical Engineers I (in Japanese), 443–444.

Paidoussis, M.P., 2003. Fluid-Structure Interactions, Slender Structures and Axial Flow, vol. 2. Elsevier-Academic Press, London (Chapter 11).

Watanabe, Y., Suzuki, S., Sugihara, M., Sueoka, Y., 2002a. An experimental study of paper flutter. Journal of Fluids and Structures 16, 529–542.

Watanabe, Y., Suzuki, S., Sugihara, M., 2002b. A theoretical study of paper flutter. Journal of Fluids and Structures 16, 543–560.

Yadykin, Y., Tenetov, V., Levin, D., 2001. The flow-induced vibration of a flexible strip hanging vertically in a parallel flow—Part 1: Temporal aeroelastic instability. Journal of Fluids and Structures 15, 1167–1185.

Yamaguchi, N., Sekiguchi, T., Yokota, K., Tsujimoto, Y., 1999a. Fluttering behavior of a flexible thin sheet in hight-speed flow (2nd Report). Transactions of the Japan Society of Mechanical Engineers (in Japanese) 65B (632), 1232–1239.

Yamaguchi, N., Yokota, K., Tsujimoto, Y., 1999b. Flutter behavior of a flexible thin sheet in high-speed flow (1st Report). Transactions of the Japan Society of Mechanical Engineers (in Japanese) 65B (632), 1224–1231.

Yamaguchi, N., Ito, K., Ogata, M., 2003. Flutter limits and behaviors of flexible webs having a simplified basic configuration in high-speed flow. ASME Journal of Fluids Engineering 125, 345–353.

Yoshida, K., 1997. Dynamic analysis of sheet deformation using spring-mass-beam model. Transactions of the Japan Society of Mechanical Engineers (in Japanese) 63C (615), 3926–3932.